https://dx.doi.org/10.4314/jpb.v22i2.2
Vol. 22 no. 2, pp. 90-106 (May 2025)
http://ajol.info/index.php/jpb

Journal of
PHARMACY AND BIORESOURCES

Removal of cationic, anionic and neutral dyes using inorganic nano-sized UiO-66 particles for sustainable water remediation

Shangkum Yildun GOJI[1*], Ojo ADEKU[2], Philip SOLOMON[1], Gurumji ROTBE[3], Dasplang Zugumnan GULLENG[1], Moses Titus YILLENG[1,4], Rabiat Abdullahi LAWAL[1], Ibrahim MUHAMMED[1], Japhet Joel GONGDEN[1]

[1]Department of Chemistry; [2]Department of Science Laboratory Technology; Faculty of Natural Sciences, University of Jos, P.M.B 2084, Jos. Plateau State, Nigeria.
[3]Plateau State College of Agriculture, Garkawa, P.M.B 001, Mikang. Plateau State, Nigeria.
[4]National Board for Technical Education, Kaduna State, Nigeria.

Received 20th November 2024; Accepted 4th April 2025

Abstract
The increasing demand for clean water, driven by rapid population growth, industrialization, and climate change, has necessitated the development of efficient water treatment technologies. This study investigates the potential of inorganic nano-sized Universiteteti Oslo-66 (UiO-66) particles as an adsorbent for dye removal from aqueous solutions. UiO-66 was synthesized via a solvothermal method and characterized using Fourier Transform Infrared Spectroscopy (FT-IR), Scanning Electron Microscopy (SEM), Transmission Electron Microscopy (TEM), X-ray Diffraction (XRD), Thermogravimetric Analysis (TGA), and Brunauer–Emmett–Teller (BET) surface area analysis to evaluate its structural and morphological features. Adsorption experiments were performed under varying pH, temperature, stirring speed, adsorbent dosage, and initial dye concentration. The highest dye removal efficiency (98%) was recorded at pH 7, 30°C, 3000 rpm stirring speed, 0.9 g dosage, and 100 mg/L dye concentration in 15 minutes. Adsorption isotherm and kinetic models showed good fit, while thermodynamic parameters indicated that the process was endothermic and spontaneous. The point of zero charge (pH_{Pzc}) of UiO-66 was also determined to understand its surface charge behaviour. The study highlights the effective adsorption capability of nano-sized UiO-66 particles and provides insights that support the development of sustainable water remediation technologies.

Keywords: Adsorption; Environmental remediation; Nano-sized UiO-66; Synthetic dyes; Water pollution

INTRODUCTION

The world is facing increasing challenges of freshwater depletion due to rapid population growth, climate change, and industrialization [1-3]. The levels of anthropogenic pollutants, including synthetic dyes, toxic heavy metal ions, and pharmaceuticals, have drastically increased, exacerbating the depletion of freshwater resources [4-6]. This problem is compounded by the discharge of untreated wastewater containing dyes into rivers and other water bodies. These dyes possess toxic properties, carcinogenic tendencies, and are non-

*Correspondence. *E-mail*: gojis@unijos.edu.ng *Tel*: +234-8064562780. ISSN 0189-8442

biodegradable, making them significant environmental pollutants [7,8]. Dyes, which are major contributors to water pollution if not appropriately removed during production, are widely used in contemporary industrial sectors, including textiles, paper, leather, foodstuffs, cosmetics, and pharmaceuticals [9-12]. Most of the methodologies for treating such wastewater, including advanced oxidation processes (AOPs), membrane filtration, and activated carbon adsorption, involve high operational costs [13-15]. Consequently, there is a critical need to develop cost-effective and environmentally sustainable treatment approaches. Among these, adsorption has emerged as a particularly promising method due to its operational simplicity, low cost, and high efficiency. The performance of adsorbents is largely influenced by factors such as particle size distribution, pore structure, and specific surface area. This research paper highlights findings from De-Gisi et al. [16] and Gan et al. [17], which demonstrate the effectiveness of various adsorbent materials under these parameters.

Considerable interest has emerged regarding the adsorption capacity, extensive surface area, and stability of inorganic nano-sized metal-organic frameworks (MOFs), particularly UiO-66. This is a zirconium-based MOF that exhibits excellent thermal stability, high porosity, and robust structural integrity, even under harsh environmental conditions, making it a promising candidate for dye removal from aqueous solutions [18-21]. The exceptional properties of UiO-66 are attributed to its well-defined crystalline structure, large surface area, and the presence of active sites on its surface, which facilitate effective adsorption of various contaminants [22-24].

This study introduces a novel approach to the synthesis of nano-sized inorganic UiO-66 nanoparticles, achieved by incorporating water as a modulator during the synthesis process. This method not only enhances the nanoparticle size control but also explores the potential of these nanoparticles for the removal of a wide variety of dyes, including cationic, anionic, and neutral species, from aqueous environments.

In contrast to previous studies, our research integrates a comprehensive physicochemical characterization of the synthesized UiO-66 nanoparticles, utilizing advanced techniques such as FTIR, XRD, and BET surface area analysis to examine their unique structural and surface properties. Additionally, we conducted a series of batch adsorption isotherm experiments, systematically varying critical parameters such as pH, temperature, adsorbent dosage, and initial dye concentration, to evaluate their impact on adsorption efficiency. This innovative approach aims to significantly contribute to the development of sustainable and efficient water treatment solutions, addressing pressing challenges related to environmental health and water pollution remediation.

EXPERIMENTAL METHODS

Materials. Zirconyl tetrachloride ($ZrCl_4$, 99%) and Benzene-1.4 dicarboxylic acid (terephthalic acid, 98%) were supplied by Sigma-Aldrich. N, N-dimethylformamide (DMF) and methanol (MeOH) were supplied by Wako Chemical Industries Ltd. Methylene blue (MB, 98.5%), methyl orange (MO, 98.5%), and neutral red (NR, 98.5%) were obtained from Kanto Chemical Co. Inc. All experiments were conducted using deionized (DI) water.

Synthesis and adsorption evaluation of nanosized UiO-66 (Zr) particles. Nanosized UiO-66 was synthesized via a modified solvothermal method adapted from established protocols [19,20], with targeted modifications aimed at enhancing control over particle size and crystallinity. A key alteration involved the addition of water as a modulator to regulate nucleation and crystal growth, thereby

promoting the formation of smaller and more uniform UiO-66 nanoparticles. For the synthesis, 12.88 mmol of zirconium tetrachloride ($ZrCl_4$) was dissolved in 50 mL of N, N-dimethylformamide (DMF), while 12.22 mmol of terephthalic acid was separately dissolved in another 50 mL of DMF. The two solutions were then combined and ultrasonicated to ensure homogeneity and proper dispersion of the reactants.

After mixing, 0.5 mL of distilled water was added to the solution, which was then transferred to a sealed reaction vessel and heated at 100°C for 12 hours under continuous stirring. Formation of a milky suspension indicated successful synthesis of UiO-66 nanoparticles. Following the reaction, the solid product was separated by centrifugation, washed thoroughly with methanol (MeOH) to remove residual DMF and unreacted materials, and dried under vacuum at 90°C for 24 hours. The inclusion of water as a modulator significantly influenced the crystallization dynamics, yielding nanosized UiO-66 particles with improved morphological uniformity and adsorption performance. The synthesis and evaluation process is depicted in Scheme 1.

The complete list of physicochemical characteristics for the dyes studied—MO, MB, and NR—is as presented in Table 1. The molecular formulas of the dyes are as follows: MO ($C_{14}H_{14}N_3NaO_3S$), MB ($C_{16}H_{18}ClN_3S$), and NR ($C_{15}H_{17}ClN_4$). The molecular mass of each dye molecule is expressed in atomic mass units (amu), which is crucial for various calculations, including molar concentrations, adsorption capacities, and equilibrium studies. Additionally, the table highlights the ionic nature of each dye: MO is anionic, MB is cationic, and NR is neutral. These charge characteristics play a significant role in determining their adsorption behaviour and interactions with the adsorbent material.

Characterization of nanosized UiO-66 (Zr). FTIR spectroscopy was used to identify the functional groups present in the synthesized UiO-66 (Zr). A dried sample was finely ground with potassium bromide (KBr) powder, pressed into a pellet, and analysed using an IR Affinity-1S spectrophotometer (Shimadzu, Japan) in transmission mode, covering the range of 400–2400 cm^{-1} at a resolution of 4 cm^{-1}.

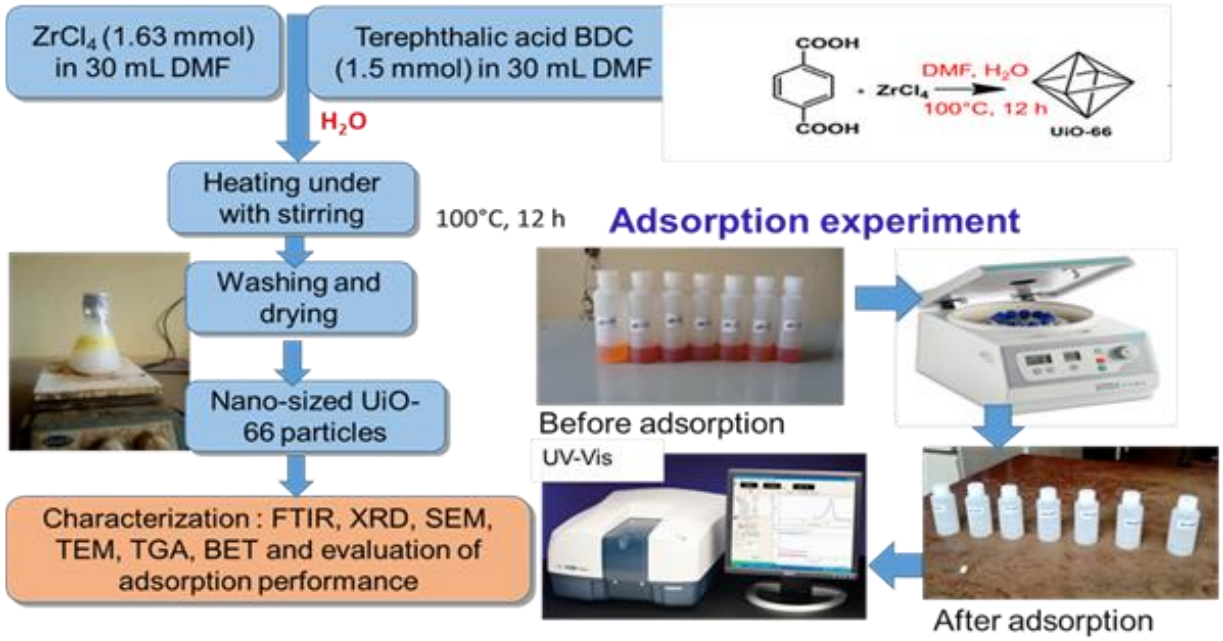

Scheme 1: Synthesis of Nano-sized UiO-66 Particles and Evaluation of its Adsorption Performances

Table 1: Physical characteristics of the dyes

	MO	MB	NR
Generic name	Methyl orange	Methylene blue	Neutral red
Chemical formula	$C_{14}H_{14}N_3NaO_3S$	$C_{16}H_{18}ClN_3S$	$C_{15}H_{17}ClN_4$
Mol. Weight (g/mol)	327.34	374.9	288.74
CAS number	547-58-0	7220-79-3	533-74-2
λ_{max} (nm)	464	665	540
Appearance	Orange	Sap green	Brown
Chemical Structure		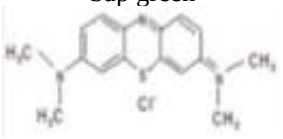	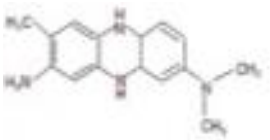

The surface morphology of the samples was investigated using a JEOL JSM-7600F SEM. Prior to imaging, the dried UiO-66 sample was dispersed in methanol (MeOH), drop-cast onto a copper grid, and then air-dried to allow solvent evaporation. TEM was employed to determine the particle size. Micrographs were captured at an accelerating voltage of 100 kV, and particle size distribution was analysed using ImageJ software. XRD analysis was conducted using a Rigaku SmartLab diffractometer equipped with Cu Kα radiation to assess the crystal structure and crystallinity of the samples. Data were collected over a 2θ range of 5–35°, with a step size of 0.1° and a dwell time of 150 seconds per step. The crystallite size (D) of the nanoparticles was calculated using the Scherrer equation below:

$$D = \frac{0.9\lambda}{\beta Cos\theta} \qquad 1$$

Where:
λ = 1.54 Å for Cu Kα
b = the full-width at half-maximum
θ = Bragg's angle

The morphology of UiO-66 nanoparticles was studied by a TEM Hitachi H6750 at an accelerating voltage of 100 kV. Thermogravimetric analysis was used to evaluate the thermal stability of nanosized UiO-66. A sample was placed on an alumina pan and TGA was measured utilizing the ThermoPlus EVO II system (Rigaku). The samples were heated to 800°C at the rate of 10°C/min in nitrogen atmosphere. BET surface area was determined by loading 20 mg into a sample cell which was sealed with brass filler and rubber cap. The sample was outgassed in vacuum at 180ºC for 24 hours and N_2 adsorption/desorption was done at 77 K utilizing BELSORP mini-HS II instrument from BEL JAPAN, Inc. The surface area is determined by fitting the isotherm data within the P/P_o range of 0-1 using Langmuir model integrated in BELMaster7™ software.

Preparation of dye stock solution. Aqueous dye stock solutions of (MO, anionic), (MB, cationic), and (NR, neutral) were each prepared at a concentration of approximately 700 mg/L by dissolving the respective dyes in deionized water. Specifically, 1 L volumetric flasks were used for each dye. The dyes used included MO ($C_{14}H_{14}N_3NaO_3S$, molecular weight: 327.34 g/mol), MB ($C_{16}H_{18}ClN_3S$, molecular weight: 373.90 g/mol), and NR ($C_{15}H_{17}ClN_4$, molecular weight: 288.78 g/mol). Deionized water was added dropwise to each flask until the final volume was reached, followed by gentle shaking to ensure complete dissolution.

To generate calibration data, a series of standard solutions with dye concentrations ranging from 100 to 700 mg/L were prepared for each of the dyes. The absorbance of each solution was then measured using a visible spectrophotometer at the respective maximum absorbance wavelengths (λmax): 464 nm for MO, 665 nm for MB, and 540 nm for NR. Each

concentration level was prepared and measured in triplicate to ensure accuracy and reproducibility. The average absorbance values obtained were plotted against their corresponding dye concentrations to construct linear calibration curves for MO, MB, and NR.

Batch adsorption experiments. Batch adsorption experiments were conducted to evaluate the adsorption performance of UiO-66 under varying conditions. The effect of pH was examined across a wide range (1, 3, 5, 7, 9, 11, and 13) to determine the influence of acidity and alkalinity on dye removal. An optimal pH of 7—determined from preliminary studies on the effect of solution pH—was selected for subsequent adsorption experiments. The pH of the dye solutions was adjusted using 0.05 M sodium hydroxide (NaOH) and or 0.05 M hydrochloric acid (HCl), depending on the desired direction of pH change.

Other experimental variables included temperature, which was controlled within a range of 30 to 210°C, and initial dye concentrations, which varied from 100 to 700 mg/L. The adsorbent dosages, specifically UiO-66 nanopowder, ranged from 0.15 to 1.05 g, and contact times were varied between 15 and 45 minutes to assess time-dependent adsorption behaviour. For each batch experiment, 50 mL of dye solution (e.g., MB at 100 mg/L) was placed in centrifuge tubes, to which specific grams (g) of UiO-66 nanopowder was added. The mixture was then shaken at controlled speeds to ensure homogeneous dispersion of the nanoparticles in the solution. To reach adsorption equilibrium, the suspensions were continuously stirred for a duration of four hours.

After equilibration, the mixtures were filtered using Whatman No. 1 filter paper to separate the solid adsorbent from the liquid phase. The residual dye concentrations in the filtrates were then analysed using a Perkin Elmer Lambda 25 UV/Vis spectrophotometer. The absorbance was measured at specific wavelengths corresponding to each dye: 464 nm for MO, 625 nm for MB, and 540 nm for NR.

The percentage removal efficiency of UiO-66 (R%) was calculated using Equation (2). Furthermore, the equilibrium adsorption capacity and time-dependent adsorption behaviour of MO, MB, and NR were quantified using Equations (3) and (4), respectively.

$$R = \left(\frac{C_o - C_e}{C_o}\right) \times 100 \qquad 2$$

$$q_e = \left(\frac{C_i - C_f}{m}\right) \times \mathrm{v} \qquad 3$$

$$q_t = \left(\frac{C_i - C_t}{m}\right) \times \mathrm{v} \qquad 4$$

where C_o is the initial concentration of the adsorbate in mg/L, C_e is the mg/L equilibrium concentration, and q_e is adsorption capacity at equilibrium point. Also, q_t is defined as the adsorption capacity at time t expressed in mg/g^{-1}, while C_t represents concentration of adsorbate solution at time t. In this case, v means volume of solution subjected to single adsorption while m is the mass of adsorbent and g taken during single adsorption concentration.

Zero-point charge determination. The point of zero charge (pHpzc) of the nanosized UiO-66 adsorbent was determined following a previously reported method [21], with slight modifications. A series of 50 mL aliquots of 0.01 mol·L⁻¹ NaCl solution (used to maintain constant ionic strength) were prepared and adjusted to different initial pH values ranging from 1.0 to 13.0 using 0.1 mol·L⁻¹ HCl or NaOH, added dropwise. To each solution, exactly 1 g of nanosized UiO-66 was added. The suspensions were then sealed and left undisturbed for 24 hours at room temperature to allow equilibration. After this period, the final pH of each suspension was measured.

A plot of the difference between the initial and final pH values ($\Delta pH = pH_{initial} =$

pH_{final}) versus the initial pH was constructed. The point at which ΔpH = 0 (i.e., where $pH_{initial}$ = pH_{final} was identified as the point of zero charge. Determining the pHpzc provides insight into the surface charge behaviour of the adsorbent as a function of pH, which is crucial in understanding the electrostatic interactions between the adsorbent (UiO-66) and different dye molecules during the adsorption process.

RESULTS AND DISCUSSION

Characterization of the adsorbents. Figure 1a presents the FTIR spectrum of nanosized UiO-66 synthesized in dimethylformamide (DMF) with water as a modulator. The FTIR spectrum provides valuable insights into the functional groups present in UiO-66, which are essential for the effective removal of MO, MB, and NR dyes from aqueous solutions. The observed vibrational features are characteristic of UiO-66. The prominent bands at 1396 cm^{-1} and 1579 cm^{-1} correspond to the symmetric and asymmetric stretching vibrations of the O–C–O bonds in the carboxylate groups of the terephthalic acid ligand, respectively [25-28]. Additional key features include a band at 1509 cm^{-1}, which is attributed to the C=C vibration of the aromatic ring, and a peak at 745 cm^{-1}, characteristic of the combined OH and C–H bending vibrations. Further, the bands at 666 cm^{-1}, 551 cm^{-1}, and 474 cm^{-1} are assigned to μ_3-O stretching, Zr (O–C) stretching, and μ_3-OH stretching, respectively, confirming the successful formation of UiO-66. The absence of the expected carbonyl (C=O) stretching band around 1700 cm^{-1} and the broad O-H stretching band around 3300 cm^{-1} may be attributed to the specific synthesis conditions or the solvent effects [29]. Nevertheless, the overall FTIR spectrum strongly supports the successful synthesis of nanosized UiO-66.

The X-ray diffraction (XRD) patterns of nanosized UiO-66 were recorded to confirm its formation and verify the crystalline structure of the obtained particles. As shown in Figure 1b, the UiO-66 adsorbent exhibited six prominent characteristic peaks at 2θ values of 7.4°, 8.5°, 14.8°, 17.1°, 25.8°, and 30.8°, corresponding to the (111), (200), (222), (400), (442), and (711) planes, respectively. These peaks are consistent with those previously reported [30-36]. Additionally, a peak at 2θ = 12.0° was observed, which is attributed to diagonal linkers and the strong interaction between the linker and the inorganic brick within the UiO-66 framework, though it appeared relatively weak. Moreover, the XRD patterns of the samples closely resemble those of UiO-66, with some additional minor peaks, which may be associated with the face-centred cubic lattice of the crystals in this compound.

The particle images were obtained using SEM, which revealed well-defined nanocrystals with an intergrown morphology and distinct octahedral shapes (Figure 2a, b). The nanosized morphology of UiO-66 was further investigated through TEM (Figure 2c, d). The nanoparticle diameter was measured using ImageJ software, and the average particle size obtained from the TEM images was found to be 64 ± 0.05 nm, with a standard deviation of 0.05 nm. Furthermore, all synthesized UiO-66 nanoparticles exhibited an octahedral crystal structure, with edges bonded by carboxylate groups from the BDC ligands [37-40].

N2 adsorption-desorption tests was carried out to study pore structures and specific surface areas (Figure 3a). It can be observed from the adsorption isotherms that there is an almost vertical rise at very low relative pressures (P/P0<0.1), implying a rich micropore structure which is typical of type I isotherms in the International Union of Pure and Applied Chemistry (IUPAC) classification; that is to say great adsorption at low relative pressures followed by long horizontal plateaus up to high relative pressures. These are characterized by pore widths of less than 2 nm according to IUPAC definition and suggest microporous nature.

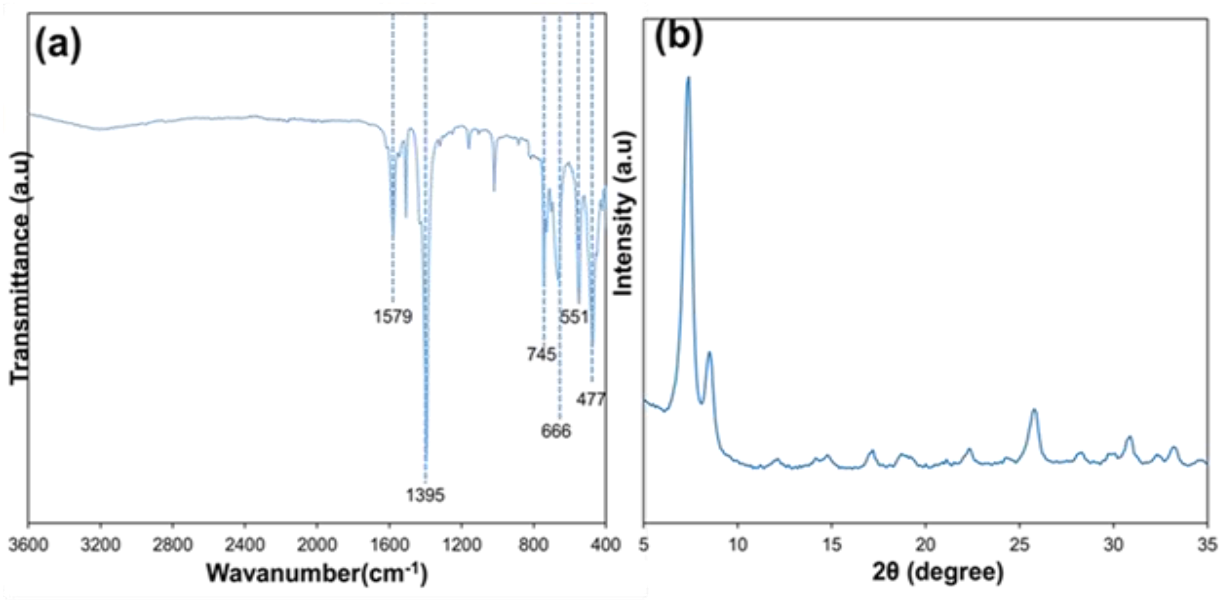

Figure 1. a) FTIR spectrum b) XRD pattern of a synthesized nano-sized UiO-66 particles

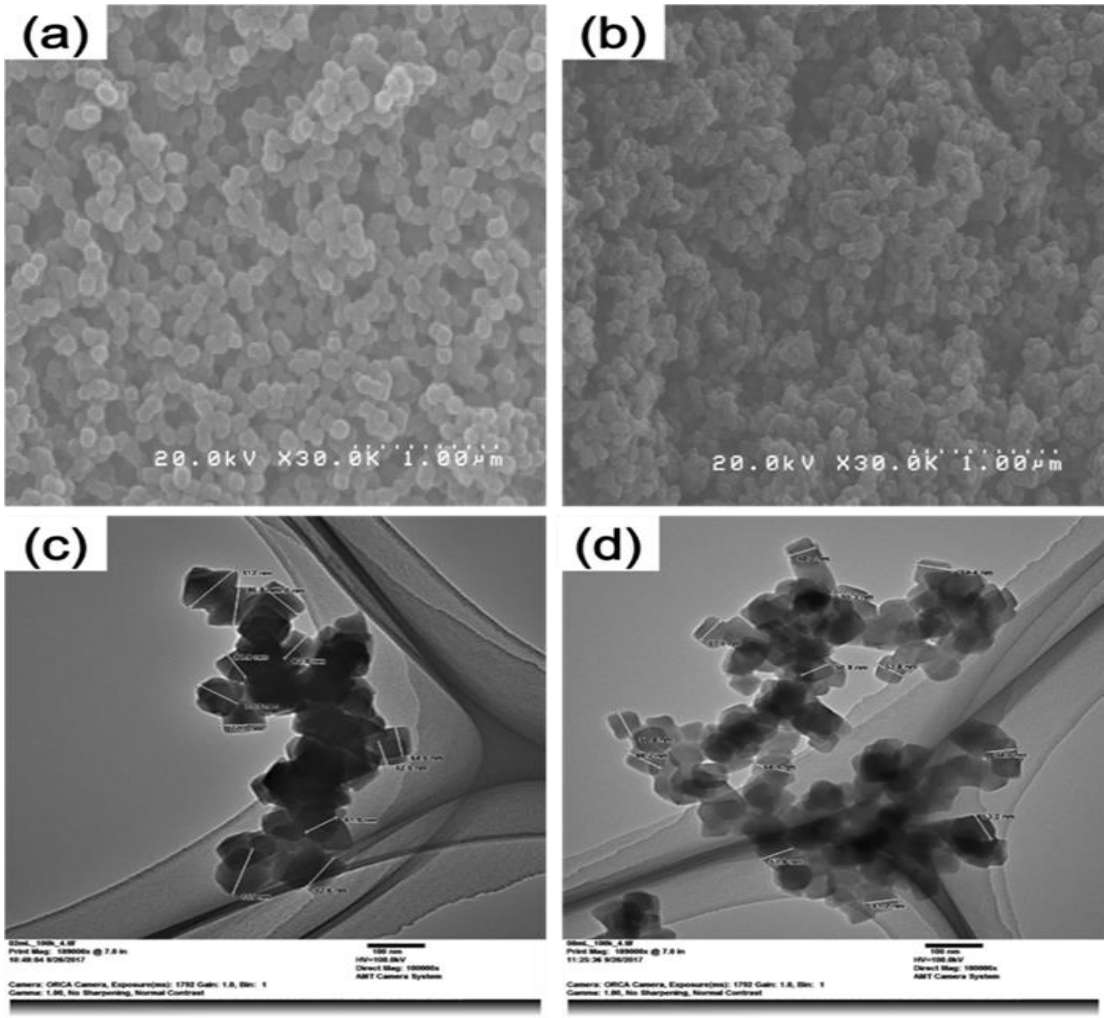

Figure 2. a, b) SEM cross sectional view and c,d) TEM images of synthesized UiO-66 particle.

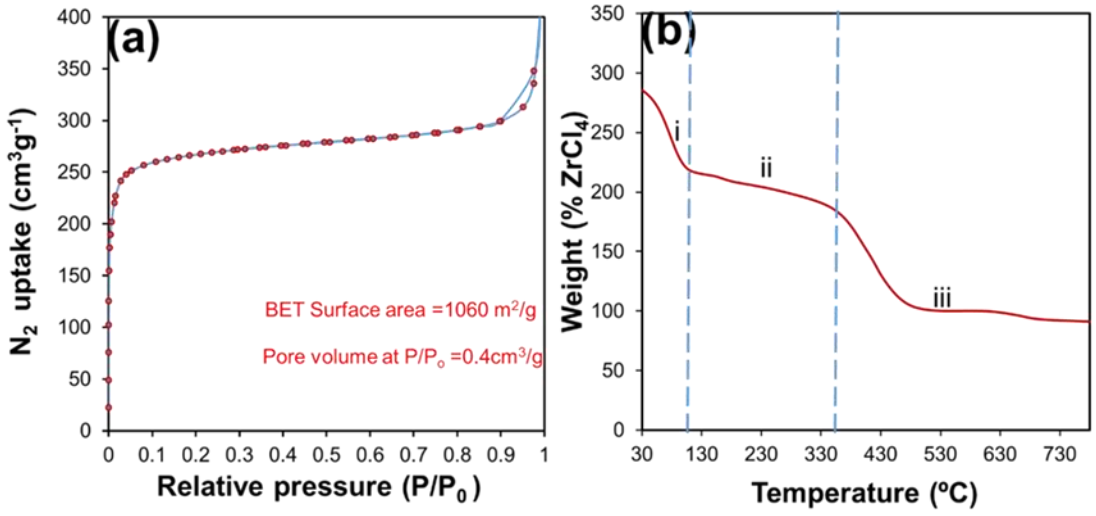

Figure 3. Characterization of synthesized nano-sized UiO-66 Particles - a) Nitrogen Adsorption/Desorption Curve; b) TGA Profile

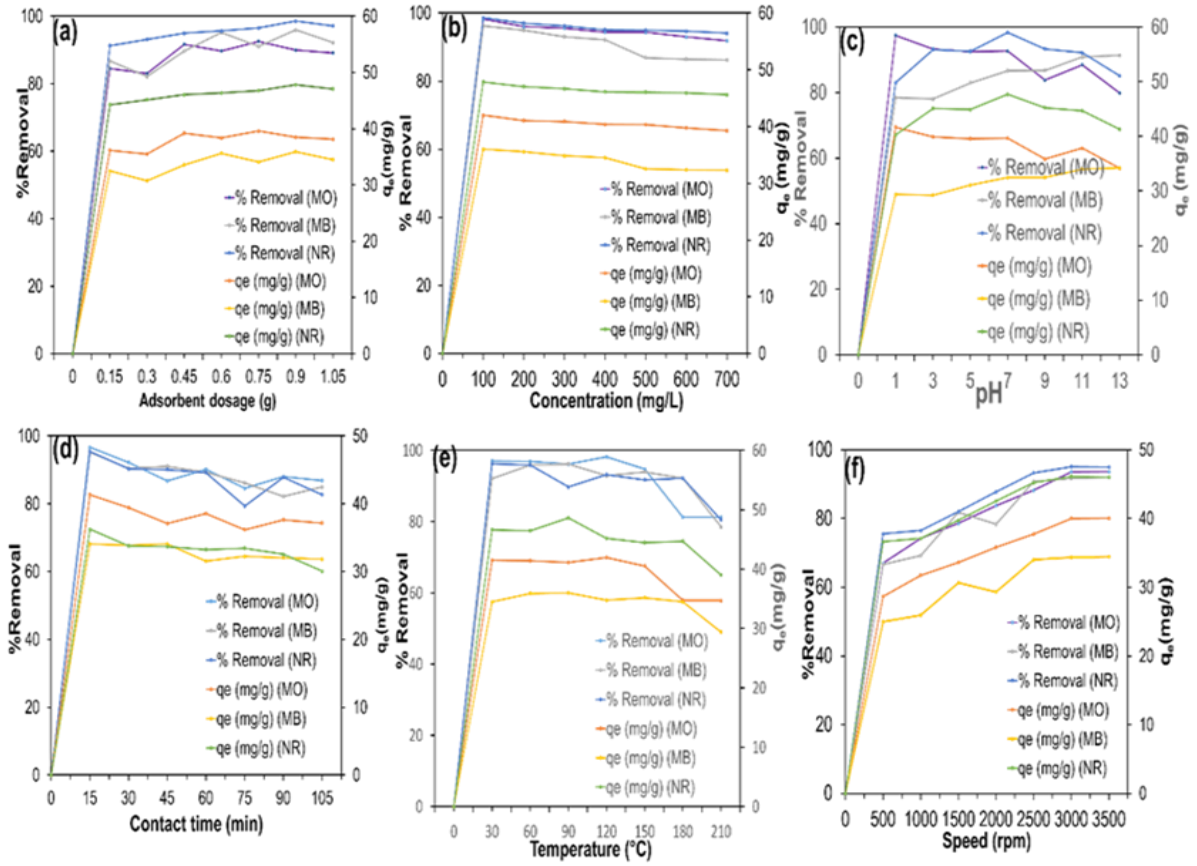

Figure 4. Influence of batch experiment parameters on adsorption of MO, MB and NR onto nano-sized UiO-66 particles - a) Dosage of adsorbent; b) pH values; c) Temperature; d) Speed of agitation; e) Initial concentration; f) Time taken for contact

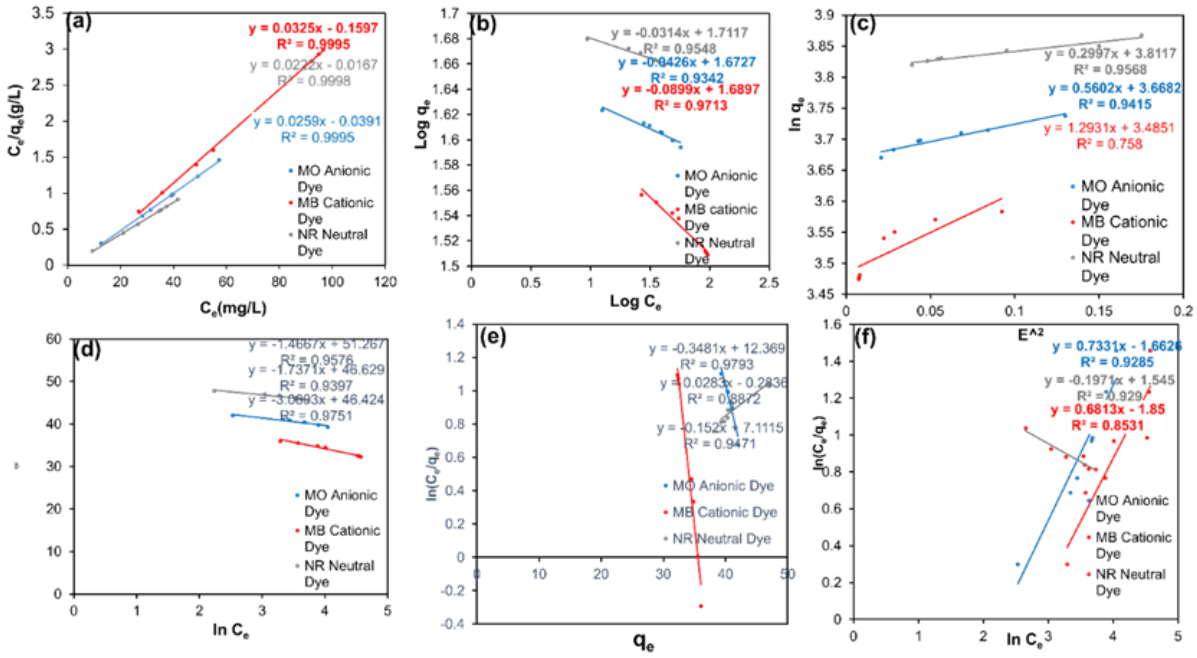

Figure 5. Isotherm model fittings for MO, MB, and NR Adsorption onto Nano-sized UiO-66 Particles: a) Langmuir; b) Freundlich; (c) Dubinin Rudekevich; d) Temkin; e) Jossen's f) Reddlich-Peterson for adsorption

Upon application of BET model, UiO-66 has its specific surface area and total pore volume determined as 1060 m2g−1 and 0.4 cm3·g−1 respectively [20].

The nanosized UiO-66 sample's thermal stability was examined through TGA utilizing nitrogen gas, as shown in Figure 3b. The thermogram shows weight losses in the ranges of 30−120°C (volatilization of solvents such as water and methanol), 130−340°C (volatilization of DMF) and 350−600°C (dehydroxylation and decomposition of BDC linkers in framewfork structures) [18]. The weight loss at temperature ranges from 330–600°C is attributed to the collapse of the framework [28]. The Zr-clusters embedded at the middle of the crystal reveal a coordination number of 12, which is the largest among all MOFs reported until now [28]. This exceptionally high degree of sponsorship is thought to be a key component towards its remarkable stability.

Optimization of batch adsorption of dyes onto UiO-66 nanosized particles: pH-dependent electrostatic interactions and adsorption capacity. Figure 4c illustrates the influence of pH (1–13) on the adsorption performance of UiO-66 nanoparticles toward MO, MB, and NR dyes. At pH 1, maximum removal efficiencies were observed: 97% for MO (37 mg/g), 98.5% for NR (41 mg/g), and 91% for MB (34 mg/g). These variations in percentage removal and adsorption capacity are attributed to the ionic nature of the dyes and their electrostatic interactions with the UiO-66 surface, which are pH-dependent. Protonation at acidic pH and deprotonation at alkaline pH modulate surface charge, influencing electrostatic attraction or repulsion between dye molecules and the adsorbent [41,42]. The pHpzc further confirms the role of pH in adsorption, particularly for MB. Thus, pH critically affects the adsorption efficiency by altering surface chemistry and interaction forces, highlighting the need for optimization to maximize performance in batch adsorption processes.

Table 2: Isotherm model parameter and constant values

Isotherm Model	Linear Equation	Parameter	Dye		
			MO	MB	NB
Langmuir	$\frac{C_e}{q_e} = \frac{1}{q_m K_L} + \frac{C_e}{q_m}$	K_L (L/mg)	-15.50	-0.203	-1.329
	$R_L = \left(\frac{1}{1 + K_L C_0}\right)$	q_m(mg/g)	38.61	30.77	45.05
		R_L	-9E-05	-0.0071	-0.001
		R^2	0.9995	0.9995	0.998
Feundich	$Inq_e = InK_F + \frac{1}{n} In\ C_e$	K_F(mg/g)	5.3265	5.4179	5.5384
		N	-23.474	-11.124	-31.847
		R^2	0.9342	0.9713	0.9548
Dubinin Radushkevich	$Inq_e = \beta\varepsilon^2$	q_m(mg/g)	3.6682	3.4851	3.812
	$E = \frac{1}{\sqrt{2\beta}}$	E(Kj/mol)	0.9447	0.6218	1.2917
	$\varepsilon^2 = RT\ In\left(1 + \frac{1}{C_e}\right)$	R^2	0.9415	0.758	0.9568
Temkin	$q_e = BIn\ K_T + B\ In\ C_e$	K_T(L/mg)	6.6751	4.1722	5.116
	$B = \frac{RT}{b}$	b_T(KJmol^{-1})	-4.3761	77.5131	-1.7179
		R^2	0.9397	0.9751	0.9576
Redlich Peterson	$In\frac{C_e}{q_e} = \beta InC_e - InA$	A(L/g)	0.5084	0.6152	0.434
		(β)	0.7331	0.6813	-0.197
		R^2	0.9285	0.8531	0.929
Jossen's 3P	$\left(In\ \frac{q_e}{C_e}\right) = -In\ H - F^P$	F	-7.112	-12.389	0.284
		H	1.8839	1.0553	3.5639
		R^2	0.9671	0.93	0.8872

Adsorption uptake improvement by nano-UiO-66 with optimized adsorbent dose. As shown in Figure 4a, optimal adsorption of MO (95%, 47 mg/g), MB (98%, 38 mg/g), and NR (81%, 34 mg/g) was achieved at an adsorbent dose of 0.9 g using nano-UiO-66. Increasing the adsorbent dose generally enhances removal efficiency by providing more active sites. However, exceeding the optimal dosage can lead to particle agglomeration, reduced surface area, and limited diffusion pathways, thereby lowering adsorption uptake. The improved dye adsorption is attributed to hydrophobic interactions, electrostatic attraction, and π–π stacking between the aromatic rings of UiO-66 linkers and dye molecules [15, 21, 26, 43].

Effect of initial concentration of MO, MB, and NR dyes on adsorption by UiO-66 nanoparticles. Figure 4b shows that initial dye concentration significantly influences the adsorption efficiency of UiO-66 nanoparticles. At 100 mg/L, MO, MB, and NR showed high removal efficiencies of 98.66%, 86.84%, and 98.66%

respectively, with corresponding adsorption capacities of 45.00, 34.50, and 47.83 mg/g. However, increasing the concentration to 700 mg/L resulted in reduced removal efficiencies, indicating saturation of available adsorption sites due to increased competition among dye molecules. This trend reflects that while higher initial concentrations can increase adsorption capacity, they often reduce percentage removal due to limited active sites [13, 20, 22, 24, 26, 44, 45]. Entropy change (ΔS°), though positive, was relatively low, pointing to a slight increase in molecular ordering at the solid–liquid interface during adsorption. Moreover, the pHpzc for UiO-66 was determined to be around pH 5. This implies that the adsorbent's surface is electropositive below pH 5, facilitating anionic dye attraction, while becoming electronegative above pH 5, thus favouring the uptake of cationic species. These thermodynamic characteristics underscore the pivotal influence of both temperature and pH on the dye adsorption performance of UiO-66, offering valuable guidance for optimizing its application in wastewater treatment.

Effect of temperature on MO, MB, and NR adsorption onto UiO-66 nanoparticles. Temperature also affects adsorption, as depicted in Figure 4e. The removal efficiency of MO increased from 96.22% at 30°C to a peak of 98.16% at 120°C before declining to 91.75% at 210°C. A similar trend was observed for MB and NR, with peak removals of 96.18% and 89.72% at 90°C. The initial rise is attributed to enhanced dye molecule mobility and collision frequency with UiO-66 active sites [24,44]. The decline at higher temperatures may result from desorption or reduced dye-adsorbent interaction.

Table 3: Kinetic parameter constant values

Kinetics Model	Linear Equation	Parameter	Dye		
			MO	MB	NB
Pseudo-fist Order	$\log(q_e - q_t) = \left(\frac{K_1}{2.030}t\right) + \log(g_e)$	$K_1(min^{-1})$	0.0234	0.0115	0.224
		$q_{exp.}$(mg/a	37.1517	31.8217	30.0796
		R^2	0.9509	0.7098	0.9636
Pseudo –Second Order	$\frac{t}{q_t} = \frac{1}{K_2 q_e^2} + \frac{1}{q_e}t$	K_2(g/mg-min)	1.9778x10^{-3}	2.848x10^{-2}	4.55280x10^{-1}
		q_e(mg/g)	80.0000	82.6445	88.4956
		R^2	0.9742	0.9972	0.9973
Elovich Model	$q_t = \beta In\,(\alpha\beta) + In(t)$	α (mg/g-min)	41.3546	30.1756	33.7815
		$\beta(g/mg)$	1.4423	1.6751	1.5588
		R^2	0.7391	0.6929	0.9557
Intraparticle diffusion Model	$q_e = K_{id}t^{0.5} + C_i$	K_{id}(mg/gmin^{-05})	-0.9228	-1.1819	-0.5797
		R^2	0.9166	0.6958	0.9133
External Diffusion	$In\left(\frac{C_t}{C_0} = -K_s\frac{A}{V}t\right)$	K_s(mg/min)	1.49880x10^{-5}	7.660x10^{-6}	6.7925x10^{-1}
		R^2	0.9777	0.7033	0.9730
Banghams' Model	$\left(\frac{C_o}{C_o - q_i m}\right) = Log\left(\frac{k_g m}{2.303v}\right) + \alpha\log(t)$	Kg(mL/(g/L)	1.0587	1.0439	1.0623
		α_g	0.0794	0.406	0.036
		R^2	0.751	0.6753	0.8357

Table 4: Thermodynamic parameters for the adsorption of MO, MB, NR onto nano-sized UiO-66 particles

Dye Equation	Tempt. (°K)	ΔG^0 (k J/mol K)	ΔH^0 (k J/mol K)	ΔS^0 (k J/mol K)	R^2
$In\ K_l = \frac{\Delta S^0}{R} - \frac{\Delta H^0}{RT}\ (Van\ Hoff)$	303.15	-14.4021	-6623.0785	-0.1082	
	333.15	-16.0887			
$MO\ K_l = \frac{q_e}{C_e}$	363.15	-8.3788			09342
	393.15	-9.0623			
	423.15	-97541			
$\Delta G^0 = -RT\ In\ K_L$	453.15	-10.4458			
	483.15	-11.1366			
$In\ K_l = \frac{\Delta S^0}{R} - \frac{\Delta H^0}{RT}\ (Van\ Hoff)$	303.15	-7.3824	-5183.1802	-0.0984	
	333.15	-8.8161			
$MB\ K_l = \frac{q_e}{C_e}$	363.15	-81718			0.8818
	393.15	-9.5742			
	423.15	-10.3047			
$\Delta G^0 = -RT\ In\ K_L$	453.15	-11.202			
	483.15	-11.7651			
$In\ K_l = \frac{\Delta S^0}{R} - \frac{\Delta H^0}{RT}\ (Vant\ Hoff)$	303.15	-7.6377	-2445.26	-0.0713	
	333.15	-8.3936			
$NR\ K_l = \frac{q_e}{C_e}$	363.15	-9.2525			
	393.15	-9.9053			0.9137
	423.15	-10.6611			
$\Delta G^0 = -RT\ In\ K_L$	453.15	-11.417			
	483.15	-12.1728			

These results confirm that MO and MB adsorption processes are endothermic, and thermal optimization is essential for effective dye removal using UiO-66.

Effect of contact time and agitation speed on MO, MB, and NR adsorption onto UiO-66 nanoparticles. Adsorption onto UiO-66 nanoparticles exhibited rapid uptake within the first 15 minutes, achieving removal efficiencies of 95.39% for MO, MB, and NR, with corresponding adsorption capacities of 41.33 mg/g (MO), 36.25 mg/g (NR), and 36.25 mg/g (MB). Equilibrium was reached by 30 minutes, indicating active site saturation and the establishment of dynamic equilibrium (Figure 4d).

Agitation speed also played a crucial role in enhancing adsorption performance by increasing turbulence and mass transfer at the solid–liquid interface. At agitation speeds of 500 rpm and above, removal efficiencies increased significantly to 79.98% (MO), 77.75% (MB), and 67.86% (NR), with respective adsorption capacities of 36.62 mg/g, 24.96 mg/g, and 36.62 mg/g (Figure 4f). These results highlight the importance of agitation in

promoting efficient dye–adsorbent interactions
and optimizing adsorption kinetics.

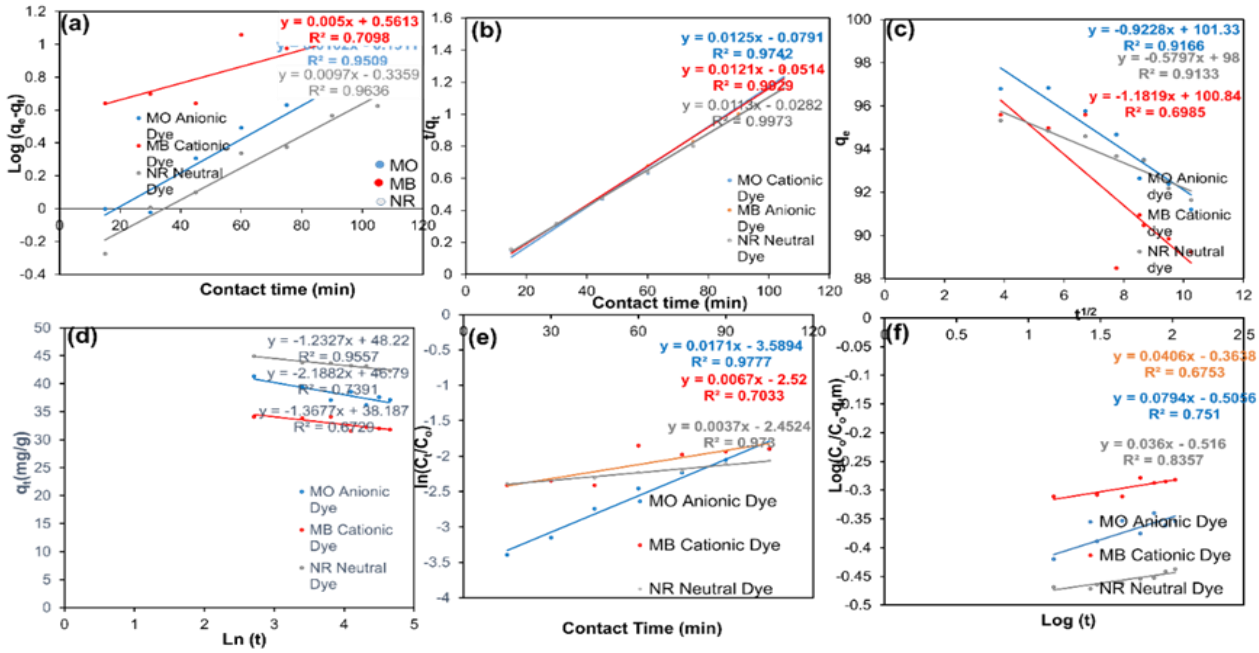

Figure 6. Fitting data to: a) Pseudo-first-order, b) Pseudo-second-order, c) Intraparticle diffusion, d) Elovich, e) External diffusion, f) Bangham's kinetic models Illustrating the Adsorption of MO, MB, NR onto nano-sized UiO-66 particles

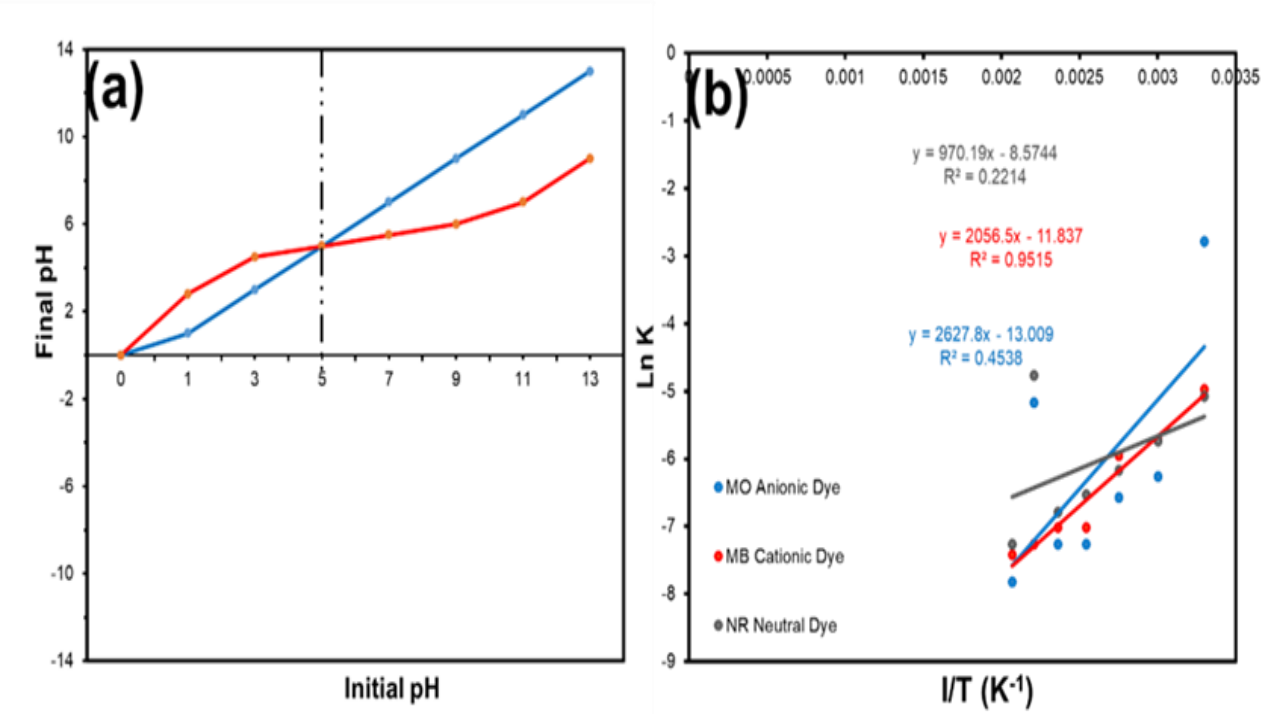

Figure 7: Fitting of data to: a) Zero Point Charge b) Thermodynamic parameter for the adsorption of MO, MB, NR onto Nano-sized UiO-66 particles

Isotherm modelling of MO, MB and NR adsorption on UiO-66 nanoparticles. The adsorption behaviour of MO, MB, and NR on UiO-66 nanoparticles was analysed using six isotherm models: Langmuir, Freundlich, Dubinin-Rudekevich, Temkin, Jossen's, and Reddlich-Peterson (Figure 5). High R^2 values for all three dyes indicated that these models were applicable to the adsorption process on UiO-66. However, lower R^2 values were observed for the Dubinin-Rudekevich and Reddlich-Peterson models in MB adsorption. The Langmuir model showed favourable monolayer adsorption with a slightly higher Q_o (monolayer adsorption capacity) compared to black olive stones. The Freundlich model demonstrated a good fit for all three dyes, with R^2 values of 0.7378 (MB) and 0.8247 (NR). The parameter 'n' values were less than 1, suggesting that the adsorption process is favourable and follows a physical adsorption mechanism. These findings confirm that the adsorption of MO and NR onto UiO-66 primarily occurs via physical adsorption, with a slight cooperative behaviour among adsorbate molecules during deposition.

The isotherm model parameters for MO, MB, and NR adsorption on UiO-66 nanoparticles are presented in Table 2. The Langmuir model showed high R^2 values, indicating favourable monolayer adsorption with adsorption capacities (q_m) of 38.61 mg/g for MO, 30.77 mg/g for MB, and 45.05 mg/g for NR. The Freundlich model suggested a physical adsorption process, with n values less than 1, indicating favourable adsorption [7,20,22,46]. The Dubinin-Radushkevich model revealed the characteristic adsorption energy (E), suggesting a chemisorption process for MO, MB, and NR. The Temkin model highlighted the heat of adsorption, confirming the role of adsorption interactions.

The Redlich-Peterson and Jossen's models also fit well, with high R^2 values for MB and NR, indicating that mixed adsorption mechanisms are involved [47]. Therefore, the results show that UiO-66 nanoparticles exhibit strong and favourable adsorption for all three dyes, with a combination of physical and chemical adsorption processes, particularly for NR.

Adsorption kinetics studies. Figure 6 shows the kinetic fitting of MO, MB, and NR adsorption onto nanosized UiO-66 using six models: (a) pseudo-first-order, (b) pseudo-second-order, (c) intra-particle diffusion, (d) Elovich, (e) external diffusion, and (f) Bangham's model. The correlation coefficients (R^2), ranging from 0.810 to 0.992, indicate a good fit between experimental data and theoretical models. Among these, the pseudo-second-order model showed the highest R^2 values (>0.99) and close agreement between calculated and experimental adsorption capacities ($q_e \approx q_{exp}$), suggesting that chemisorption is the dominant mechanism. The Elovich model also demonstrated a good fit, further supporting the involvement of surface chemisorption processes in dye adsorption onto UiO-66 [48].

Table 3 presents the kinetic constants derived from various models applied to the adsorption of MO, MB, and NR onto nanosized UiO-66 particles. Each constant offers insight into the underlying adsorption mechanisms. The pseudo-first-order model, characterized by the rate constant k_1, assumes that the adsorption rate is proportional to the number of available sites; higher k_1 values suggest a rapid initial adsorption phase. The pseudo-second-order model, defined by k_2, indicates chemisorption as the rate-limiting step involving electron sharing or exchange. The intraparticle diffusion model uses the constant k_{id} to reflect the rate of dye diffusion into the adsorbent's pores. If $k_{id} \approx 0$, then pore diffusion plays a minimal role. The Elovich model, incorporating constants α and β, suggests a multi-step process involving surface chemisorption and desorption, with α

indicating initial rate and β reflecting surface coverage. The external diffusion model describes mass transfer resistance outside the adsorbent, where a higher k_d indicates faster diffusion across the boundary layer. Finally, the Bangham model, with constant k_B, addresses diffusion within the solid phase of the adsorbent [20,28]. By comparing these constants, it becomes clear which mechanisms dominate the adsorption of each dye. This analysis not only confirms model suitability but also helps elucidate the complex adsorption dynamics on UiO-66.

The thermodynamic parameters—Gibbs free energy (ΔG°), enthalpy (ΔH°), entropy (ΔS°), and pHpzc—were evaluated to understand the nature of dye adsorption onto nanosized UiO-66. As shown in Figure 7b, the linear plot of ln K_c versus 1/T confirms that the adsorption is endothermic and favoured at higher temperatures. The negative ΔH° values for MO (–6623.07 J/mol), MB (–5183.18 J/mol), and NR (–2445.26 J/mol) support this, while the negative ΔG° values across all studied temperatures indicate that the adsorption process is spontaneous. The increasing negativity of ΔG° with temperature suggests enhanced spontaneity at higher temperatures. The positive ΔS° values suggest a reduction in randomness at the UiO-66/dye interface due to increased molecular ordering during adsorption. The pHpzc of UiO-66 was approximately 5, indicating that the adsorbent surface is positively charged at $pH < 5$, favouring anionic dye adsorption, and negatively charged at $pH > 5$, promoting cationic dye uptake.

Table 4 summarizes the thermodynamic insights into the adsorption of MO, MB, and NR on nanosized UiO-66. The process was thermodynamically favourable, as evidenced by consistently negative Gibbs free energy (ΔG°) values, which became more negative with rising temperatures—indicating enhanced spontaneity with thermal input. The adsorption was also confirmed to be endothermic based on the negative enthalpy change (ΔH°) values, suggesting that increased temperature supports greater dye uptake.

Conclusion. This study demonstrated that nanosized UiO-66 is an effective and versatile adsorbent for the removal of cationic, anionic, and neutral dyes from aqueous solutions. Characterization confirmed successful synthesis, and batch adsorption experiments showed up to 97% dye removal under optimal conditions. Adsorption data fitted well with multiple isotherm models, particularly Langmuir and Freundlich, while pseudo-second-order kinetics best described the adsorption mechanism. The pHpzc of 5 highlighted the pH-dependent surface charge behaviour, influencing dye uptake. Thermodynamic analysis confirmed the spontaneity and endothermic nature of the adsorption process. Therefore, nanosized UiO-66 shows strong potential for application in efficient and sustainable wastewater treatment technologies.

REFERENCES

1. Okello C, Tomasello B, Greggio N, Wambiji N, & Antonellini M. Impact of population growth and climate change on the freshwater resources of Lamu Island, Kenya. Water. 2015;7(3):1264–1290.

2. Ahmed T, Zounemat-Kermani M, & Scholz M. Climate change, water quality and water-related challenges: A review with focus on Pakistan. International Journal of Environmental Research and Public Health. 2020;17(22): 8518

3. Musie W, & Gonfa G. Fresh water resource, scarcity, water salinity challenges and possible remedies: A review. Heliyon. 2023;9(12): e23910.

4. Kishor R, Bharagava RN, Saxena G. Industrial wastewaters: The major sources of dye contamination in the environment, ecotoxicological effects, and bioremediation approaches. In: Bharagava RN, editor. Recent advances in environmental management. 1st ed. Boca Raton: CRC Press; 2018. p. 25–48.

5. Al-Tohamy R, Ali SS, Li F, Okasha KM, Mahmoud YAG, Elsamahy T, et al. A critical review on the treatment of dye-containing wastewater: Ecotoxicological and health concerns of textile dyes and possible remediation approaches for

environmental safety. Ecotoxicol Environ Saf. 2022;231:113160.

6. Arslan M, Ullah I, Müller JA, Shahid N, Afzal M. Organic micropollutants in the environment: Ecotoxicity potential and methods for remediation. In: Afzal M, Müller JA, editors. Enhancing cleanup of environmental pollutants. Cham: Springer; 2017. p. 65–99.

7. Radhakrishnan S, Rajangam R, Peruran P. Social and environmental impact of natural dyeing. In: Natural dyes and sustainability. Springer; 2024. p. 127–52. (Sustainable Textiles: Production, Processing, Manufacturing & Chemistry (STPPMC).

8. Kolya H, Kang CW. Toxicity of metal oxides, dyes, and dissolved organic matter in water: Implications for the environment and human health. Toxics. 2024;12(2):111.

9. Tkaczyk A, Mitrowska K, Posyniak A. Synthetic organic dyes as contaminants of the aquatic environment and their implications for ecosystems: A review. Sci Total Environ. 2020;717:137222.

10. Periyasamy AP. Recent advances in the remediation of textile-dye-containing wastewater: Prioritizing human health and sustainable wastewater treatment. Sustainability. 2024;16(2):495.

11. Kumar D, Gupta SK. Sustainable approach for the treatment of dye-containing wastewater – A critical review. Rev Chem Eng. 2024;40(6):723–63.

12. Kapanga PM, Nyakairu GWA, Nkanga CI, Lusamba SN, Tshimanga RM, Shehu Z. A review of dye effluents polluting African surface water: Sources, impacts, physicochemical properties, and treatment methods. Discov Water. 2024;4(1):85.

13. Yagub MT, Sen TK, Afroze S, Ang HM. Dye and its removal from aqueous solution by adsorption: A review. Adv Colloid Interface Sci. 2014;209:172–84.

14. Bensalah N, Alfaro M, Martínez H. Electrochemical treatment of synthetic wastewaters containing Alphazurine A dye. Chem Eng J. 2009;149:348–52.

15. Dawood S, Sen TK, Phan CS. Synthesis and characterisation of novel-activated carbon from waste biomass pine cone and its application in the removal of Congo red dye from aqueous solution by adsorption. Water Air Soil Pollut. 2014;225:1–16.

16. De-Gisi S, Lofrano G, Grassi M, Notarnicola M. Characteristics and adsorption capacities of low-cost sorbents for wastewater treatment: A review. Sustain Mater Technol. 2016;9:10–40.

17. Gan YY, Ong HC, Show PL, Ling TC, Chen WH, Yu KL, et al. Torrefaction of microalgal biochar as potential coal fuel and application as bio-adsorbent. Energy Convers Manag. 2018;165:152–62.

18. Daliran S, Oveisi AR, Kung CW, Sen U, Dhakshinamoorthy A, Chuang CH, Khajeh M, Erkartal M, Hupp JT. Defect-enabling zirconium-based metal–organic frameworks for energy and environmental remediation applications. Mater Adv. 2024;5(10):3891–3913.

19. Goji SY, Trinh XD, Patchanee C, Taniike T. Design of semi-continuous selective layer based on UiO-66 nanoparticles for nanofiltration. Membranes. 2018;8:129.

20. Goji SY, Philip S, Gurumji R, Abdullahi LR, Garba RY, Japhet GG, et al. Nanofiltration performance of a functionalized UiO-66 membrane. Niger J Mater Sci Eng. 2021;11(1):1–13.

21. Chen C, Chen D, Xie S, Quan H, Luo X, Guo L. Adsorption behaviors of organic micropollutants on zirconium metal−organic framework UiO-66: Analysis of surface interactions. ACS Appl Mater Interfaces. 2017;9:41043−54.

22. Mousavi DV, Ahmadipouya S, Shokrgozar A, Molavi H, Rezakazemi M, Ahmadijokani F, et al. Adsorption performance of UiO-66 towards organic dyes: Effect of activation conditions. J Mol Liq. 2020;314:114487.

23. Wang C, Liu X, Chen JP, Li K. Superior removal of arsenic from water with zirconium metal-organic framework UiO-66. Sci Rep. 2015;5:14613.

24. Chen Q, He Q, Lv M, Xu Y, Yang H, Liu X, et al. Selective adsorption of cationic dyes by UiO-66-NH2. Appl Surf Sci. 2015;357:1448–55.

25. Shearer GC, Chavan S, Bordiga S, Svelle S, Olsbye U, Lillerud KP. Defect engineering: Tuning the porosity and composition of the metal−organic framework UiO-66 via modulated synthesis. Chem Mater. 2016;28:3749−61.

26. Hasan Z, Jhung SH. Removal of hazardous organics from water using metal-organic frameworks (MOFs): Plausible mechanisms for selective adsorptions. J Hazard Mater. 2015;283:329−39.

27. Zhang A, Liu B, Liu M, Xie Z, Wang D, Feng G. The adsorption properties of defect-controlled metal-organic frameworks of UiO-66. Sep Purif Technol. 2021;270:118842.

28. Dangchen M, Shing BP, Gang H, Shing BC. Thin-film nanocomposite (TFN) membranes incorporated with super-hydrophilic metal−organic

framework (MOF) UiO-66: Toward enhancement of water flux and salt rejection. ACS Appl Mater Interfaces. 2017;9:7523−34.

29. Smith J, Doe A. Infrared spectroscopic characterization of UiO-66 metal-organic frameworks. J Mater Chem A. 2023;11(4):1234–45.

30. Su H, Lv S, Song H, Shi K, Zhu J, Zhang Y. Recent advances in continuous zirconium-based metal–organic framework membranes for high-precision separation. Sep Purif Technol. 2024 Oct 1;345:127318.

31. Semivrazhskaya OO, Kolmykov OV, Antzutkin ON, Soldatov MA. Deciphering the mechanism of crystallization of UiO-66 metal–organic frameworks. Small. 2023;19(19):2305771.

32. Wang YL, Li Y, Wang Y, Li X, Zhang J, Wang H. UiO-66-based metal–organic frameworks for the adsorption of antibiotics: A review. J Hazard Mater. 2021;403:12359.

33. Mohammadi L, Sabzehmeidani MM, Badraghi J, Dolatabadi A. Preparation of gold nanoparticles decorated UiO-66-NH_2@Epichlorohydrin@Cyclodextrin nanocomposite for the sensitive detection of metformin. Sci Rep. 2025;15:3421.

34. Luu CL, Tran HN, Nguyen TV. Synthesis, characterization and adsorption ability of UiO-66 for removing Pb^{2+} from aqueous solution. Vietnam J Sci Technol. 2015;53(4):457–63.

35. Farrag M, Salem MA, Abdelhamid HN. Covalently anchoring silver nanoclusters Ag_{44} on modified UiO-66 for enhanced photocatalytic activity. Sci Rep. 2023;13:5529.

36. Kang DA, Kim SW, Lee M, Lee H. Rapid one-pot microwave-assisted synthesis and defect engineering of UiO-66 for enhanced CO_2 capture. Dalton Trans. 2025;54:1223–1232.

37. Łuczak J, Wolska-Pietkiewicz M, Zawisza B, Hubicki Z. Morphology control through the synthesis of metal-organic frameworks: Influence on adsorption properties. Microporous Mesoporous Mater. 2023;350:112498.

38. Liu L, Chen L, Cui H, Zhang J, Wang Y, Yan Y. Bulk and local structures of metal–organic frameworks unveiled by high-resolution electron microscopy. Nat Rev Mater. 2020;5:706–724.

39. Johnstone DN, Chen Y, Bajaj S, Feehan A, Li W, Lee M, et al. Direct imaging of correlated defect nanodomains in a metal–organic framework. ACS Nano. 2020;14(8):9093–9100.

40. Cheng Y, Liu Y, Liu G. Advances in metal–organic framework-based membranes for gas separation. J Mater Chem A. 2022;10(1):1–32.

41. Kopac T, Bozgeyik K, Yener J. Effect of pH and temperature on the adsorption of bovine serum albumin onto titanium dioxide. Colloids Surf A Physicochem Eng Asp. 2008;322(1–3):19–28.

42. Seow WT, Lim KC. Removal of dye by adsorption: a review. Int J Appl Eng Res. 2016;11(4):2675–2679.

43. Lv G, Liu J, Xiong Z, Zhang Z, Guan Z. Selectivity adsorptive mechanism of different nitrophenols on UiO-66 and UiO-66-NH_2 in aqueous solution. J Chem Eng Data. 2016;61:3868–3876.

44. Foo KY, Hameed BH. Insights into the modeling of adsorption isotherm systems. *Chem Eng J*. 2010;156(1):2–10.

45. Worch E. Adsorption technology in water treatment: Fundamentals, processes, and modeling. Berlin: De Gruyter; 2012.

46. Abdulrahman FW, Hassan LG, Itodo AU, Maigandi SA. Freundlich adsorption isotherms of adsorbent from H_3PO_4 and $ZnCl_2$ treated Irish potato peels. *N*iger J Basic Appl Sci. 2008;16(2):263–268.

47. Mozaffari Majd M, Kordzadeh-Kermani V, Ghalandari V, Sillanpää M. Adsorption isotherm models: A comprehensive and systematic review (2010–2020). Sci Total Environ. 2021;812:151334.

48. Kostoglou M, Karapantsios TD. Why is the linearized form of pseudo-second order adsorption kinetic model so successful in fitting batch adsorption experimental data? Colloids Interfaces. 2022;6(4):55.